AIAA 2003-0218

Flow Control Analysis on the Hump Model with RANS Tools

Sally A. Viken, Veer N. Vatsa,
Christopher L. Rumsey, and Mark H. Carpenter
NASA Langley Research Center
Hampton, VA

41st Aerospace Sciences Meeting & Exhibit
6-9 January 2003
Reno, NV

FLOW CONTROL ANALYSIS ON THE HUMP MODEL WITH RANS TOOLS

Sally A. Viken*
NASA Langley Research Center, Mail Stop 170, Hampton, VA 23681

Veer N. Vatsa***, Christopher L. Rumsey***†, Mark H. Carpenter**
NASA Langley Research Center, Mail Stop 128, Hampton, VA 23681

ABSTRACT

A concerted effort is underway at NASA Langley Research Center to create a benchmark for Computational Fluid Dynamic (CFD) codes, both unstructured and structured, against a data set for the hump model with actuation. The hump model was tested in the NASA Langley 0.3-m Transonic Cryogenic Tunnel. The CFD codes used for the analyses are the FUN2D (Full Unstructured Navier-Stokes 2-Dimensional) code, the structured TLNS3D (Thin-Layer Navier-Stokes 3-Dimensional) code, and the structured CFL3D code, all developed at NASA Langley. The current investigation uses the time-accurate Reynolds-Averaged Navier-Stokes (RANS) approach to predict aerodynamic performance of the active flow control experimental database for the hump model. Two-dimensional computational results verified that steady blowing and suction and oscillatory suction/blowing can be used to significantly reduce the separated flow region on the model. Discrepancies do exist between the CFD results and experimental data in the region downstream of the slot with the largest differences in the oscillatory cases. Overall, the structured CFD codes exhibited similar behavior with each other for a wide range of control conditions, with the unstructured FUN2D code showing moderately different results in the separated flow region for the suction and oscillatory cases.

LIST OF SYMBOLS

c	chord length
c_f	section skin friction coefficient
C_P	pressure coefficient
c_μ	steady blowing momentum coefficient, J/cq
$<c_\mu>$	oscillatory blowing momentum coefficient, $= h/c(\rho_j'(u_j')^2)/q$ (CFD) $= h/c(1 + T_\infty/T_j)(<u'>/U_\infty)^2$ (experimentally)
f	frequency [Hz]
F^+	reduced frequency, $= f\, x_{sep}/U_\infty$
GN_2	Gaseous Nitrogen
h	slot height
J	momentum at slot, $= \rho_j h U_j^2$
M_∞	free-stream Mach number
p	pressure
q	freestream dynamic pressure, $= 1/2\rho_\infty U_\infty^2$
Re	Reynolds number
Re_x	Reynolds number based on x location
T	Temperature
t	time
U,u	averaged and fluctuating velocity
x/c	normalized streamwise location
x_{sep}	distance from separation to reattachment
y_{min}	distance from wall to first grid point
y^+	law of the wall variable

$$y^+ = \mathrm{Re}^* y_{\min}\sqrt{\frac{c_f}{2.}}$$

η	normal direction to surface
ρ	density
ξ	tangential direction to surface
ω	angular frequency

Abbreviations:

BDF	Backwards Differentiation Formulae
BLC	Boundary Layer Control
CFD	Computational Fluid Dynamics
DES	Detached Eddy Simulation
L.S.	Lower Surface
QA	Quality Assurance
RANS	Reynolds-Averaged Navier-Stokes
<>	phase locked values
2-D	Two-Dimensional
3-D	Three-Dimensional

* Flow Physics and Control Branch
** Computational Modeling and Simulation Branch
† Senior Member AIAA
†† Associate Fellow AIAA

Subscripts:

aw	adiabatic wall
j	condition at blowing slot
∞	free-stream condition

Superscripts:

( )′	denotes root mean square of fluctuating component

BACKGROUND

Much attention has been devoted to the development of techniques capable of enhancing our ability to control steady and unsteady flows for a wide variety of applications.[1,2] A number of active flow control concepts have been tested in the laboratory and in flight. These concepts have included dynamic stall control using a deformable leading edge[3], separation control with mechanical siren-type actuator[4] and piezoelectric devices[5], separation control with pulsed vortex generator jets[6], zero-net-mass oscillation separation control,[7-12] and thrust vectoring using zero-net-mass oscillatory actuation.[13]

Computational studies[14-16] have demonstrated that RANS methodologies can effectively predict performance gains obtained with active flow control. Although quantitative agreement is often lacking between the computational and experimental results, one study using a structured-grid incompressible RANS code has shown good quantitative agreement with experimental results for an isolated zero-net-mass actuator.[17] The current effort investigates the potential use of the RANS approach to predict aerodynamic performance for active flow control applications, expanding on earlier work at LaRC.[18-20] A comprehensive set of experimental data is available for the hump model tested in the 0.3-m Transonic Cryogenic Tunnel at NASA LaRC. Previous CFD work has been conducted on the hump model using 2-D RANS, hybrid RANS-LES, and 3-D LES.[21-23] However, all simulations were performed with much lower Reynolds numbers than conducted experimentally, and also no turbulent calculations were presented for suction or oscillatory suction/blowing cases.

EXPERIMENT

Although conducting the experiment was not part of this effort, some relevant background information about the 0.3-m tunnel and hump model will be discussed.

The 0.3-m Transonic Cryogenic Tunnel

Testing of the hump model was conducted in the 2-D adaptive-wall test section of the 0.3-m Transonic Cryogenic Tunnel. The tunnel is a continuous-flow, single-return, fan-driven transonic wind tunnel that uses nitrogen gas as the test medium. This tunnel is capable of operating at stagnation temperatures from 78 - 327K, and stagnation pressures from 1.2 - 6.0 atmospheres.[24] The fan speed is variable so that the empty test section Mach number can be varied continuously from approximately 0.10 to 0.95.

The tunnel test section is 0.3 m by 0.3 m at the entrance, with all four walls being solid.[25] The sidewalls are rigid, whereas the top and bottom walls are flexible and can be moved. The flexible tunnel walls are 1.82 m long and are anchored at the upstream end. The rear 0.4-m portion of the flexible tunnel walls diverges at 4.1° to form a transition between the test section and the high-speed diffuser. The test section has a streamlining length of 1.43 m. The center of the model-mounted turntable is located 0.79 m downstream of the test section entrance. Each flexible wall is supported by a system of 21 jacks. For the hump model experiment, the floor and ceiling of the tunnel were diverged in the vicinity of the model to reduce blockage resulting from the boundary layer growth on the test section walls.

Model

The nominally 2-D "hump" model, with c = 200 mm, simulates the upper surface of a 20% thick modified Glauert Glas II airfoil[10] (figure 1). The leading edge was faired smoothly between x/c = -0.05 to 0.05 in order to eliminate a slope discontinuity and local separation at the leading edge. The geometry of the forward part of the model subjects the boundary layer to both a favorable pressure gradient as well as streamwise convex curvature. A moderate favorable pressure gradient exists up to ~55% of the chord followed by a severe adverse pressure gradient, imposed by the highly convex surface at x/c ≈ 0.65, that then relaxes towards the trailing edge. Without flow control, the flow separates at the highly convex region of the model (x/c = 0.65) and a large turbulent separation bubble is formed. Experimental results have shown that with periodic excitation applied from the slot, the size of the separation bubble was significantly reduced. Two slot locations were investigated experimentally, x/c = 0.59 and x/c = 0.64. The slots were about 0.25% chord wide (h = 0.50 mm). End plates on the model isolated the boundary layers on the floor and ceiling of the wind tunnel, thereby minimizing any spanwise flow non-uniformity over

the model. The model was equipped with one streamwise and three spanwise rows of pressure taps (figure 2). The streamwise row contained 34 pressure taps, and each spanwise row contained nine pressure taps. The pressure taps were hooked up to an Electronic Scanning Pressure (ESP) module, which sampled data at 10 Hz. The model was also instrumented with 12 dynamic pressure transducers (indicated by x symbols in figure 2), installed under the model surface. The dynamic pressure transducers were sampled at 12 KHz. The full scale of the unsteady pressure transducers was 10 psid.

Experimental Setup

Figure 3 shows a schematic description of the experimental setup in the 0.3-m tunnel.[10] The model was mounted on the right sidewall of the tunnel, where the upstream boundary layer was known to be turbulent. A rotating siren type valve was used to generate the pressure oscillations inside the model cavity. Turbine flow meters on the inlet side of the oscillatory blowing valve and on the exhaust side of the model cavity were used to measure the flow volume entering and exiting the model cavity. The mass flow entering or exiting the model cavity was determined by measuring the temperature and pressure near the flow meters in addition to the flow volume. The steady net mass flow in or out of the slot was the difference between the mass flow entering and exiting the model cavity. Steady blowing or steady suction could be applied by holding the oscillatory blowing valve in the fully open position and varying the inlet or exhaust mass flow rates. A flush mounted dynamic pressure transducer in the model cavity was used to measure the pressure fluctuations produced by the oscillatory blowing valve. These pressure oscillations could then provide an estimate of the slot exit velocities by correlating these pressure oscillations to those measured in the benchtop calibration test of the model using a hot-wire mounted on a 3-D traverse system.[10]

Experimental Uncertainty

The estimation of the uncertainty of c_μ's were within ±10% of the quoted values or 0.01 absolute value (the bigger of the two), and $\langle c_\mu \rangle$'s were within ±25% of the quoted values.[10]

COMPUTATIONAL ANALYSIS

Computational analyses have been conducted with the unstructured FUN2D and the structured TLNS3D and CFL3D codes, to assess the effectiveness of the codes for steady as well as unsteady flow control applications.

FUN2D Flow Solver

The FUN2D flow solver is a node based, implicit, upwind flow solver used for computing flows around airfoil configurations discretized with an unstructured grid.[26] The governing equations are the time-dependent Reynolds-Averaged Navier-Stokes equations in conservation-law form, which are integrated in time to obtain a steady state solution. The inviscid fluxes are obtained on the faces of each control volume by using the flux-difference-splitting (FDS) technique of Roe.[27] A node-based algorithm is used in which the variables are stored at the vertices of the mesh and the equations are solved on non-overlapping control volumes surrounding each node. The viscous terms are evaluated with a finite-volume formulation that results in a central-difference-type scheme.

For steady state computations, the solution is driven to convergence using an Euler implicit advancement in pseudo-time. For time-dependent computations, the solution is discretized in physical time with the second-order backwards differentiation formulae (BDF), while pseudo-time iterations are again employed to relax the equations. The linear system of equations resulting from either formulation is iteratively solved with a point-implicit procedure. The Spalart-Allmaras turbulence model[28] is used in this investigation and all computations assume fully turbulent flow.

TLNS3D Flow Solver

The TLNS3D code is a multiblock structured grid solver that utilizes the generalized thin-layer Navier-Stokes equations as the governing equations.[29] The spatial terms are discretized using the cell-centered finite volume scheme with artificial dissipation added for stability. Time is discretized in a fully implicit sense by using either a multistep BDF or multistage Runge-Kutta scheme. The resultant nonlinear algebraic equations are solved iteratively in pseudo-time with a multi-grid acceleration used to speed up the convergence.[30] The Spalart-Allmaras turbulence model is also used in this investigation and all computations assume fully turbulent flow.

CFL3D Flow Solver

CFL3D is a structured-grid upwind multi-zone CFD code that solves the generalized thin-layer Navier-Stokes equations. It can use point-matched, patched, or overset grids, and employs local time step scaling, grid sequencing, and multigrid to accelerate convergence to steady state. Time-accurate capability is also available, and the code can employ low-Mach number preconditioning for accuracy in computing low-speed steady-state flows. CFL3D is a finite volume method. It uses third-order upwind-biased

spatial differencing on the convective and pressure terms, and second-order differencing on the viscous terms; it is globally second-order spatially accurate. The FDS method of Roe is employed to obtain fluxes at the cell faces. It is advanced in time with an implicit three-factor approximate factorization scheme. A wide variety of eddy-viscosity turbulence models are available in the code, including nonlinear models.[31] The Spalart-Allmaras turbulence model was also used in this investigation to be consistent and all computations assume fully turbulent flow.

Unstructured Grids

The 2-D unstructured grids for the FUN2D code were generated with advancing front type point placement with iterative local re-meshing for grid quality improvement.[32-33] For the internal flow studies, the length of the tunnel wall test section ran from 0.79 m ahead of the center of the model to 0.64 m behind the center of the model. The "finest" level grid generated has 278,511 nodes. Figure 4 shows one level of the unstructured grid generated within the 0.3-m tunnel walls, which consist of 44,355 nodes. Figure 5 shows an enlarged view of the grid around the hump model.

Structured Grids

The 2-D structured grids generated with Gridgen were set up as an internal flow problem similar to that of the unstructured grid. The finest level grid has 195,456 cells and 3 (non-equal size) blocks. Figure 6 shows an enlarged view of the grid around the hump model with every other point shown for clarity.

Boundary Conditions

The boundary conditions on the hump model and the right sidewall of the tunnel corresponded to no-slip between the fluid and the solid boundary at their interface, with a constant temperature wall that was set to the adiabatic wall temperature T_{aw}. The opposite wall, the left sidewall of the tunnel, was treated as an inviscid surface. The internal "actuator" boundary was also treated as an inviscid surface for the baseline case with no control. No difference was observed between an inviscid and viscous boundary condition defined for the actuator boundary in the baseline case. For the control cases, the "actuator" boundary condition corresponded to $\rho V(\xi, \eta = 0, t) =$ Amplitude*$f(\xi)$*cos (ωt) where $f(\xi) = 1$ (tophat distribution). For inflow conditions, temperature was also specified on the "actuator" boundary from the experimental data. The side walls of the slot were modeled with no-slip boundary conditions. To obtain the boundary conditions at the tunnel inlet, the flow was assumed to be both inviscid and isentropic in this region so that quantities for the computation of the flux along the inflow boundary were obtained from two locally 1-D Riemann invariants. The Riemann invariants were considered constant along characteristics defined normal to the inflow boundary. At the downstream boundary, back pressure was specified in order to approximate the upstream conditions at the tunnel inlet. Both CFL3D and FUN2D used a back pressure of 0.9982 times reference pressure, whereas TLS3D used 0.995 times reference pressure.

DISCUSSION

Initial calculations were conducted on the hump model using the theoretical coordinates for the baseline case of $M_\infty = 0.25$, with Re = 16 million. Figure 7 shows the FUN2D results compared with experimental mean data in which the x/c = 0.64 slot insert was installed. Discrepancies can be seen between the CFD results and experimental data starting at x/c ≈ 0.40. CFD results show a favorable pressure gradient on the hump model extending back to x/c = 0.55 followed by a steep adverse pressure gradient. The flow separates and forms a large separation bubble from x/c = 0.65 to x/c = 1.21(based on skin friction results from the CFD calculations). Experimental data shows a favorable pressure gradient back to x/c = 0.5, followed by the pressure recovery starting at x/c = 0.55. A large separation bubble is formed, with the experimental estimate of separation from x/c = 0.65 to x/c = 1.21±0.05.[10] A small step in the experimental Cp distribution exists at x/c ~ 0.45 which is most likely due to the modular break-line in the model.[10] With the large differences in Cp distributions it was assumed that the theoretical coordinates were not a true representation of the model geometry. Therefore QA (quality assurance) data was taken on the model.

The QA data was obtained for the "hump" model with the x/c = 0.64 slot insert installed. This configuration was chosen because more experimental data was available for this configuration. In addition, this slot location was found to be more effective for $M_\infty \leq 0.3$.[11] Five span surveys of the model coordinates were taken with ~ 2000 data points taken along each cut at every 0.005". The QA coordinates were smoothed with a fourth-order polynomial smoothing routine. During the smoothing operation, the coordinates moved less than one tenth of one percent of the original QA geometry. Some surface discontinuities still existed in the surface geometry even after the smoothing operation. The most significant difference between the QA data and the theoretical coordinates was a larger thickness in the QA trailing edge element ahead of slot.

Figure 8 shows a comparison of the centerline QA geometry with the theoretical coordinates near the slot. Due to differences between the QA data and theoretical coordinates, the CFD analyses were conducted on the QA data and faired theoretical slot geometry. Since it was preferred not to grid the entire cavity region, approximately four slot widths inside the cavity were included in the geometry for the initial CFD analysis. For the steady blowing case, the flow through the slot was smooth, with the flow attached to the upper and lower surface of the slot walls. However, for the suction case, a large separated flow region developed on the upper surface of the slot. Due to the "actuator" boundary condition specifying a constant mass flux across the boundary, the flow was being forced to reattach to the upper slot wall near the actuator boundary. Modifications were made to the slot region in the CFD grid by moving the actuator boundary further inside the cavity and tapering the cross sectional area to obtain a more uniform flow across the boundary for both the steady blowing and suction cases. Figure 9 shows a view of the slot region used in the following calculations. The CFD grid did not model the wide cavity region in order to avoid having an area of very low Mach number flow, which can be problematic for compressible CFD solvers. By using the QA geometry and including the modified slot region, the CFD results were significantly improved in comparison with the experimental data.

Grid Convergence Study

Grid convergence studies were conducted with the codes for the baseline case of $M_\infty = 0.25$ and Re = 16 million. To ensure the sublayer of the turbulent shear flow was sufficiently resolved, a y^+ of 0.7 was chosen for the unstructured "fine" grid and $c_f = 0.455/(\ln^2(0.06Re_x))$, (reference 34), was used to determine the minimum grid spacing normal to the surface, y_{min}. For a chord Reynolds number of 16 million, the turbulent minimum normal wall spacing on the hump model was determined to be 1.0×10^{-6} based on a non-dimensional chord of 1.0. Table 1 lists the four levels of grids used in the grid refinement study with the FUN2D code. Clustering of points in the slot region was conducted for the "refine" and "fine" level grids.

Table 1. FUN2D Unstructured Grid Refinement

Grids	No. of L.S. Boundary Nodes	No. of Grid Nodes	Min. Wall Spacing
Refine	2318 (1482 model)	278,511	4.e-07
Fine	2269 (1469 model)	260,094	1.e-06
Medium	1363 (893 model)	91,062	2.e-06
Coarse	1007 (640 model)	44,355	4.e-06

Pressure distributions, y^+, and convergence history of log(Residual) were compared for the four levels of grids at the baseline case. Examining the Cp distributions in figure 10, only minor differences can be observed between the "refine" grid through the "coarse" grid. The y^+ distributions, shown in figure 11 indicate that the "refine" and "fine" grids should have sufficient resolution since both maintain a y^+ level of 0.7 or below. The convergence history of log(Residual), figure 12, shows that the residual reduces six and one-half orders or more for the "refine", "fine", and "medium" grids. The "coarse" grid reduces approximately three orders of magnitude and then levels off. The FUN2D results to be presented were calculated on the "refine" grid for the Re = 16 million cases and the "fine" grid for Re = 4.2 million cases.

Table 2 shows the two levels of grids used in the grid refinement study with the structured codes. Calculations with both structured codes were conducted with the same grids. Both "fine" and "medium" levels have a y_{min} spacing that yields a $y^+ < 0.7$.

Table 2. Structured Grid Refinement

Grids	No. of L.S. Boundary Nodes	No. of Grid Cells	Min. Wall Spacing
Fine	1018 (791 model)	195,456	4.e-07
Medium	510 (396 model)	48,864	8.3e-07

Pressure distributions and convergence history of log(Residual) are shown for the two levels of structured grids on the baseline case of $M_\infty = .25$ and

Re = 16 million for the CFL3D code in figures 13 and 14, followed by TLNS3D code results in figures 15 and 16. Minimal differences can be seen in the Cp distributions for the two grid levels with both codes. The CFL3D grid convergence history of log(Residual) show the medium grid residual reduces approximately six and one-half orders followed by the restart case on the fine grid reducing approximately three orders in magnitude. For TLNS3D, the medium grid residual reduces approximately three and one-half orders in magnitude and the fine grid reduces approximately three orders. For the structured codes, the steady state computations at Re = 16 million were conducted with the "fine" grid with all other computations conducted on the "medium" grid.

RESULTS

Computational flow analyses were conducted on the hump model for $M_\infty = 0.25$, at Re = 16 million and Re = 4.2 million. All baseline, steady suction, and steady blowing cases were run non-time-accurate, and achieved steady state convergence. Oscillatory cases were run time-accurately. Only two-dimensional computations were performed for the current study. All experimental pressure coefficient data shown in the following figures represent the mean data. Results will be presented for the baseline with no control, control with steady suction and steady blowing, and control with oscillatory suction/blowing.

Baseline (no control)

For the baseline study, no actuation was used as a precursor to the flow control simulations. Figure 17 shows the computed pressure coefficients versus the experimental data for freestream Mach number of 0.25, and Re = 16 million. Overall, good agreement with the RANS codes was achieved in the attached-flow region ahead of the slot. The slight differences between CFD codes upstream of slot are due to differences in specified back pressure at the tunnel exit. Both CFD and experimental data show that the flow decelerated as it approached the leading edge region of the airfoil, steeply accelerated up to x/c = 0.20, and then the acceleration weakened back to x/c = 0.40. Some discrepancies can be seen between the CFD results and the experimental data from x/c = 0.40 through x/c = 0.56. From the CFD results, a fairly flat Cp region exists from x/c ~ 0.40 through 0.56 where some waviness of the Cp distribution exists due to waviness in the QA geometry. The computed pressure recovery region begins at x/c = 0.56 and continues to the trailing edge of the element ahead of slot, x/c = 0.64, where the flow separates. As can be observed from figure 17, the computed pressure distribution in the separation bubble differs slightly from that found experimentally. Although the upstream boundary layer was known to be turbulent, relaminarization could have occurred in the experiment on the forward part of the model due to the very strong pressure gradient relative to the thickness of the boundary layer from x/c = 0.0 to x/c = 0.20.[35] The state and thickness of the boundary layer may not have an effect on the Cp distribution upstream of the slot, but could possibly influence the separated shear layer. Table 3 shows the separation bubble length from the CFD calculations (based on surface skin friction) and the experimental estimate of separation.[10] CFD tends to predict a somewhat larger bubble length than experiment. The FUN2D computed streamlines around the hump model for the baseline condition are shown in figure 18, where the large separation bubble can be seen.

Table 3. Separation Bubble Length for Baseline Case ($M_\infty = 0.25$, Re = 16 million)

	Separation Location (x/c)	Reattachment Location (x/c)
FUN2D	0.643	1.310
TLNS3D	0.642	1.255
CFL3D	0.643	1.283
Experiment	0.65	1.21±0.05

The lower Reynolds number of 4.2 million was also investigated for the baseline configuration. Figure 19 shows the computed pressure distributions of the CFD codes with the experimental data. Table 4 lists the separation bubble length from the CFD calculations and the experimental estimate of separation.[10] A small elongation of the bubble length was found experimentally as the Reynolds number decreased.[12] The separation bubble was also calculated to be slightly larger at Re = 4.2 million, than at Re = 16 million with all CFD codes.

Table 4. Separation Bubble Length for Baseline Case ($M_\infty = 0.25$, Re = 4.2 million)

	Separation Location (x/c)	Reattachment Location (x/c)
FUN2D	0.643	1.333
TLNS3D	0.643	1.270
CFL3D	0.643	1.304
Experiment	0.65	1.21±0.05

The effects of the incoming boundary layer thickness were investigated both experimentally and computationally. It was found experimentally that the thickness of the upstream boundary layer had only a minor effect on the flow over the model.[10-12] Even though the momentum thickness of the upstream boundary was halved in certain experimental runs, only minor changes were observed in the steady and fluctuating model pressure distributions. A boundary layer removal (BLC) system, consisting of a porous plate located between 451 mm and 273 mm upstream of the turntable center and spanning the tunnel height, was used to reduce the boundary layer thickness. Wall suction through the porous plate removed the low momentum portion of the near wall boundary layer. The boundary layer was measured 20 mm downstream of the porous plate and 50 mm below the model centerline. The effect of the tunnel BLC system on the upstream boundary layer is shown in figure 20 with corresponding pressure distributions based on the upstream boundary layer profile shown in figure 21.[36] Similar analyses were conducted computationally for M_∞ = .25 and Re = 4.2 million with the CFL3D code. An inflow profile was specified such that the velocity profile calculated at station 253 mm upstream of the turntable was similar to that found experimentally. The difference between a freestream profile (characteristic inflow boundary condition) and an inflow profile specified at the inlet is shown in figure 22, which compares the calculated velocity profiles at station 253 mm upstream of the turntable center. The corresponding pressure distributions are shown in figure 23. Based on both experimental and CFD results it was determined that the incoming boundary layer thickness does not have much effect on the separation and reattachment points. All remaining CFD computations in this paper use freestream (characteristic) inflow.

Control (steady suction and steady blowing)

As will be shown, both experimental data and CFD results indicate that both steady suction and steady blowing can be used to minimize or completely eliminate the separation bubble on the model. For the steady suction and blowing cases, the mass flow through the slot was determined in the experiment. Then, using the area of the model slot, the mass flux was calculated. A uniform mass flux at each node across the "actuator" boundary was defined to obtain the desired 2-D net mass flow through the slot. Temperature was also specified on the inflow boundary for the blowing cases based on the experimental temperature reading inside the cavity.

Steady Suction

Figure 24 shows the computed pressure coefficients along with the experimental data for M_∞ = 0.25, Re = 16 million, and c_μ = -0.76%. The mass flow prescribed into the slot was 0.0634 Kg/sec. Very good agreement can be seen between the CFD results and the experimental data ahead of the slot, but some discrepancies between all three CFD results and experimental data can be observed in the pressure recovery region. An overexpansion of the flow can be seen computationally from x/c ≈ 0.65 – 0.8 compared with that of the experimental data. Similar results are predicted in the pressure recovery region aft of the slot using the two structured codes, however a larger separation bubble is calculated with the unstructured code. The reason for this discrepancy is not known. Table 5 shows the length of the separation bubble from the CFD calculations. From experimental results, an unstable separation region was estimated to begin around x/c = 0.8, with no separation bubble length estimated.[10] Further computational investigations were conducted to see if an increased mass flow through the slot could enable the flow to withstand the pressure gradient longer and remain attached. Figure 25 shows the computational results along with the experimental data for M_∞ = 0.25, Re = 16 million, and c_μ = -1.4%. The mass flow prescribed into the slot was 0.0870 Kg/sec. A reduction in the overexpansion region is seen for the CFD results at these conditions, leading to only a slight difference between the experimental data and the CFD results at x/c ≈ 0.65 – 0.75. The FUN2D results again show a larger separation bubble being calculated than the structured code results. The separation bubble lengths for this case are defined in Table 5. Some discrepancies in the CFD results and experimental data could be due to a number of issues: 1) boundary conditions on the actuator boundary may not be specified properly, 2) turbulence model deficiencies, and 3) possibility of three-dimensional Gortler-type vortices existing in the experiment over the concave section which cannot be predicted with the two-dimensional computations[37], or other three-dimensional effects.

Table 5. Separation Bubble Length for Suction Cases(M_∞ = 0.25, Re = 16 million)

Codes	cμ[%]	Separation Location (x/c)	Reattachment Location (x/c)
FUN2D	-0.077	0.662	1.086
CFL3D	-0.077	0.666	1.032
FUN2D	-0.76	0.674	0.984
TLNS3D	-0.76	0.679	0.933
CFL3D	-.0.76	0.679	0.941
FUN2D	-1.4	0.679	0.940
TLNS3D	-1.4	0.693	0.873
CFL3D	-1.4	0.693	0.873

Steady Blowing

Computational results for two blowing cases are presented. Figure 26 shows the computed pressure coefficients along with the experimental data for M_∞ = 0.25, Re = 16 million, and c_μ = 1.68%. The prescribed mass flow out of the slot was 0.1086 Kg/sec, with the actuator boundary temperature defined at 230.95 K. Very good agreement can be seen between the CFD results and the experimental data for the hump model ahead of the slot. A strong accelerated flow region exists ahead of the slot region followed by the flow leaving the trailing edge of the element ahead of the slot and merging with the shear layer from the cavity. Only a small separation bubble near x/c = .65 is calculated with the FUN2D and CFL3D codes, as shown in Table 6. No separation bubble is calculated with the TLNS3D code. Experimental results[10] suggest that the separation region aft of the slot was completely eliminated on the model with the strong blowing. The CFD codes calculate a steep pressure recovery region back to x/c = 0.78, overpredicting the experimental data. The computational pressure recovery then relaxes; with the flow remains attached all the way back to the downstream boundary. Figure 27 shows the FUN2D computed streamlines around the hump model for the blowing case, with the flow remaining attached through the pressure recovery region.

A computational study was also conducted with a smaller blowing c_μ of 0.9%. The prescribed mass flow out of the slot was 0.0835 Kg/sec, with the actuator boundary temperature defined at 220.34 K. Even at this lower c_μ, only a small separation bubble was calculated with the CFD codes near x/c = .65 with the flow then attached all the way back to the downstream boundary. The CFD results and the experimental data for this case analyzed at M_∞ = 0.25 and Re = 16 million, with c_μ = 0.9% are presented in figure 28.

Table 6. Separation Bubble Length for Blowing Cases(M_∞ = 0.25, Re = 16 million)

Codes	cμ[%]	Separation Location (x/c)	Reattachment Location (x/c)
FUN2D	0.9	0.648	0.656
TLNS3D	0.9	0.650	0.651
CFL3D	0.9	0.650	0.651
FUN2D	1.68	0.649	0.659
TLNS3D	1.68	---	---
CFL3D	1.68	0.650	0.652

Control (oscillatory suction/blowing)

Oscillatory suction/blowing was used to control the size of the separation bubble and gradually eliminate it by increasing the amplitude. For the oscillatory cases conducted in the experiment, the span-averaged net mass flux was approximately zero, but this was not verified to be true at a specific spanwise location. A dynamic pressure transducer was installed inside the model cavity to monitor the cavity pressure fluctuations which would later be correlated with the fluctuating slot exit velocities through a benchtop calibration using compressed air outside of the tunnel.[9] As stated earlier, the estimation of uncertainty of $\langle c_\mu \rangle$ was within ±25% of the quoted values.[10]

Two sets of oscillatory cases were investigated; one at Re = 16 million, and one at Re = 4.2 million. The effect of suction with c_μ < 0.15% was found experimentally to be similar to those of oscillatory suction/blowing at comparable $\langle c_\mu \rangle$'s.[12] For example, at M_∞ = 0.25 and Re = 16 million, similar mean Cp distributions were obtained with the suction case of c_μ = -0.077% and the oscillatory case of $\langle c_\mu \rangle$ = 0.095% with F^+ = 1.6 (forcing frequency of 774 Hz), as shown in figure 29.[10] Computational analyses were conducted at M_∞ = 0.25 and Re = 16 million for the suction case of c_μ = -0.077% and a series of $\langle c_\mu \rangle$'s with F^+ = 1.6. In the experiment, the excitation frequency introduced was not a perfect sine wave[12], however this assumption was made at the "actuator" boundary during the CFD calculations. For the experimental runs at Re = 16 million, the temperature inside the cavity was a factor of ~2.5 higher that the tunnel reference temperature. When a zero-mass-flux disturbance was introduced, the blowing part of the disturbance was warm GN_2,

whereas the suction part was cold GN_2.[9] The higher temperature at the inflow was not simulated in the CFD analysis.

The computational oscillatory cases were run time-accurately at least 20 shedding cycles to set up the flow field and then the Cp's were averaged over ~ 20 cycles. The cases presented were run with 100 iterations per shedding cycle. A time-step study conducted with CFL3D (not shown) indicated no noticeable difference in averaged Cp's between 100 steps per cycle and 200 steps per cycle. An oscillatory mass flow rate was prescribed at the "actuator" boundary. The computational $<c_\mu>$'s were determined at the "actuator" boundary. Figures 30 and 31 shows the steady suction case of c_μ = -0.077% and the time-averaged Cp distributions over a range of $<c_\mu>$'s analyzed with the FUN2D code and the CFL3D codes, respectively, along with the experimental data for the corresponding forcing frequency, Mach number, and Reynolds number. Table 7 lists the peak mass flow rates across the actuator boundary, the corresponding $<c_\mu>$'s and mean separation bubble lengths calculated. The suction and oscillatory CFD results show an overexpansion region from x/c ≈ 0.65 - 0.80. Notice from figure 31 that average Cp results downstream of the slot using $<c_\mu>$ levels of 0.263% and 0.971% for oscillatory flow bracket the steady suction results of c_μ = -0.077%. With the increase in amplitude of $<c_\mu>$, the separation bubble is reduced; however CFD results do not for any $<c_\mu>$ tested show the same behavior as the mean experimental data.

Table 7. Separation Bubble Length for Oscillatory Cases(M_∞ = 0.25, Re = 16 million, F^+ = 1.6)

Codes	Peak Mass Flow (Kg/s)	$<c_\mu>$%	Sep. Location (x/c)	Reattachment Location (x/c)
FUN2D	0.032	0.027	0.651	1.264
CFL3D	0.032	0.027	0.653	1.263
FUN2D	0.064	0.111	0.655	1.235
CFL3D	0.064	0.111	0.656	1.220
FUN2D	0.097	0.263	0.658	1.196
CFL3D	0.097	0.263	0.658	1.172
CFL3D	0.160	0.971	0.685	0.911

Further analyses were conducted for a range of $<c_\mu>$'s at the Reynolds number of 4.2 million, in which the temperature inside the cavity was only a factor of ~1.15 higher that the tunnel reference temperature, therefore reducing the uncertainty of $<c_\mu>$ between the CFD results and experimental data. The CFD oscillatory cases were compared with experimental data at M_∞ = 0.25, Re = 4.2 million, and $<c_\mu>$ = 0.126%, with F^+ = 1 (forcing frequency of 788 Hz). Table 8 lists the peak mass flow rates across the actuator boundary, the corresponding $<c_\mu>$'s and mean separation bubble lengths calculated. Figures 32, 33, and 34 show the computational results for three levels of $<c_\mu>$'s analyzed with the experimental mean data at $<c_\mu>$ = 0.126%. Again, the overexpansion region calculated with the CFD codes can be observed from x/c ≈ 0.65 - 0.80. A larger mean separation bubble is calculated with the FUN2D code than both CFL3D and TLNS3D, which is consistent with previous suction results. Further investigation needs to be conducted to determine what leads to the differences between computational results and experimental data just downstream of the slot. The same CFD issues discussed earlier could be factors: 1) improper actuator boundary conditions; 2) turbulence model deficiencies; and 3) 3-D effects. The question of RANS suitability for unsteady separated flows may also be an issue.

Table 8. Separation Bubble Length for Oscillatory Cases(M_∞ = 0.25, Re = 4.2 million, F^+ = 1)

Codes	Peak Mass Flow (Kg/s)	$<c_\mu>$%	Sep. Location (x/c)	Reattachment Location (x/c)
FUN2D	0.039	0.103	0.653	1.242
TLNS3D	0.039	0.103	0.654	1.208
CFL3D	0.039	0.103	0.654	1.221
FUN2D	0.077	0.476	0.657	1.140
TLNS3D	0.077	0.476	0.661	1.086
CFL3D	0.077	0.476	0.660	1.107
CFL3D	0.110	1.185	0.703	0.880

Vorticity plots for the FUN2D and CFL3D cases analyzed at $<c_\mu>$ = 0.476% show eight phases of one actuator cycle in figure 35 and 36, respectively. Full blowing at the "actuator" boundary corresponds to 90°, whereas 270° corresponds with full suction. The no flow phases of the cycle are at 0° and 180°. An enlarged view of the slot region is represented in each phase clip to show the flow exiting the cavity and merging with the boundary layer of the element ahead of the slot. A vortex on

the downstream side of the slot was formed and convected downstream away from the surface. The two codes show similar results, although FUN2D calculations were conducted on a finer grid with better resolution.

CFD results using CFL3D show the separation bubble is significantly reduced at $<c_\mu>$ = 1.185%. A vorticity plot at this large $<c_\mu>$ shows eight phases of one actuator cycle in figure 37. Although the CFD result is at a higher $<c_\mu>$ than investigated in the experiment, it is shown here to demonstrate the unsteady mechanism that may be responsible for reducing separation. As the mass flow exits the slot, two vortices are formed and convect downstream, closer to the model surface than the $<c_\mu>$ = 0.476% case, transporting higher momentum air into the lower layers of the boundary layer and reducing the separation bubble significantly.

FUTURE WORK

Due to discrepancies between the CFD results and experimental data primarily with the suction and oscillatory cases, a follow on experiment for the hump model is planned in the 20 inch x 28 inch low-speed facility at NASA LaRC. The data obtained will be used for CFD analysis at a NASA/EFCOFTAC Workshop in the spring of 2004. A more comprehensive experimental data set will be obtained to address the issues and concerns encountered with this first CFD analysis on the hump model and to also provide the CFD community a database for the development and validation of active flow control CFD tools. Steady suction and oscillatory suction/blowing cases will be analyzed in the experiment, obtaining back pressure, and pressure fluctuations and mass flow rates as a function of time for the "actuator" boundary conditions. Internal ducting will be used to conduct the suction cases, while an acoustic type actuator will be used for the oscillatory cases. Laser Velocimetry (LV), Particle Image Velocimetry (PIV), and hot wire anemometry will be used to obtain flow field data. Profiles will be obtained at the inflow and outflow boundaries, upstream of the model, ahead of the slot and aft of the slot region to obtain as much detailed data as possible. Slot calibrations will be performed in-situ at the slot exit with hot wire anemometry. Static and unsteady pressures will be obtained with pressures also taken inside the cavity region to provide the CFD researchers as much boundary condition information as possible. CFD calculations will be conducted with 3-D unsteady RANS and Detached Eddy Simulation (DES)[38] to more accurately simulate the experiment.

SUMMARY

A concerted effort has been underway at NASA Langley Research Center to create a benchmark for CFD codes, both unstructured and structured, against the detailed data set on the hump model. The hump model was tested in the NASA Langley 0.3-m Transonic Cryogenic Tunnel. The CFD results presented in this paper were obtained from calculations made with the unstructured FUN2D code and structured TLNS3D and CFL3D codes, all developed at NASA Langley.

The investigation used the time-accurate RANS approach to predict aerodynamic performance of the active flow control experimental database for the hump model. Boundary conditions that prescribe mass flow were implemented into the CFD codes and comparisons were made between the results of the active flow control CFD model and the experimental data. Computational results verified that steady blowing and suction and oscillatory suction/blowing can be used to significantly reduce the separated flow region on the model. Overall, the structured CFD codes exhibited similar behavior with each other for a wide range of control conditions, with the unstructured FUN2D code showing moderately different results in the separated flow region for the suction and oscillatory cases. Discrepancies existed between all the CFD results and experimental data in the region downstream of the slot, with the largest difference in the oscillatory cases. These discrepancies may be due to lack of sufficient boundary condition information at the "actuator" boundary, turbulence model deficiencies, or 3-D effects. These discrepancies need to be addressed in the upcoming experiment and CFD analyses. A more comprehensive detailed data set will be obtained with the upcoming experiment followed by the CFD analysis being conducted with 3-D unsteady RANS and DES.

ACKNOWLEDGMENT

The authors are grateful to Latunia Pack and Avi Seifert for supplying the geometry and experimental data along with insightful discussions relative to the flow control experiment. The authors would also like to thank David Greenblatt for productive discussion relative to the flow control experiment.

REFERENCES

1. Gad-el-hak, M., "Flow Control," Applied Mechanics Review, Vol. 42, No. 10, 1989, pp. 261-293.

2. Gad-el-hak, M., and Bushnell. D. M., "Separation Control: Review," J. Fluids Engineering, Vol. 113, 1991, pp. 5-30.
3. Chandrasekhara, M. S., Wilder, M. C., and Carr, L. W., "Control of Flow Separation Using Adaptive Airfoils." AIAA Paper 97-0655, January 1997.
4. Seifert, A., Bachar, T., Wygnanski, I., Kariv, A., Cohen, H., and Yoeli, R., "Application of Active Separation Control to a Small Unmanned Air Vehicle," Journal of Aircraft, Vol. 36, No. 2, 1998, pp. 474-477.
5. Seifert, A., Eliahu, S., Greenblatt, D., and Wygnanski, I,. "Use of Piezoelectric Actuators for Airfoil Separation Control," AIAA Journal, Vol. 36, No. 8, 1998, pp. 1535-1537.
6. McManus, K., and Magill, J.,"Separation Control in Incompressible and Compressible Flows Using Pulsed Jets," AIAA Paper 96-1948, June 1996.
7. Seifert, A., Darabi, A., and Wyganski, I., "Delay of Airfoil Stall by Periodic Excitation," Journal of Aircraft, Vol. 33, No. 4, July-August 1996, pp. 691-698.
8. Seifert, A., and Pack, L. G., "Oscillatory Excitation of Unsteady Compressible Flows Over Airfoils at Flight Reynolds Numbers," AIAA Paper 99-0925, January 1999.
9. Seifert, A., and Pack, L. G., "Oscillatory Control of Separation at High Reynolds Numbers," AIAA Journal Vol. 37, No. 9, September 1999, pp. 1062-1071.
10. Seifert, A., and Pack, L. G., "Active Control of Separated Flows on Generic Configurations at High Reynolds Numbers," AIAA 99-3403, June-July 1999.
11. Seifert, A., and Pack, L. G., "Separation Control at Flight Reynolds Numbers: Lessons Learned and Future Direction," AIAA Paper 2000-2542, June 2000.
12. Seifert, A., and Pack, L. G., "Active Flow Separation Control on Wall-Mounted Hump at High Reynolds Numbers." AIAA Journal, Vol. 40, No. 7, July 2002.
13. Pack, L. G., and Seifert, A., "Periodic Excitation for Jet Vectoring and Enhanced Spreading," AIAA Paper 99-0672, January 1999.
14. Donovan, J.F., Kral, J. D., and Cary, A. W., "Active Flow Control Applied to an Airfoil," AIAA Paper 98-0210, January 1998.
15. Ravidran, S. S., "Active Control of Flow Separation Over an Airfoil," NASA/TM-1999-209838, December 1999.
16. Wu, J. Z., Lu, X.-Y., Denny, A. G., Fan, M., and Wu, J.-M., "Post-Stall Flow Control on an Airfoil by Local Unsteady Forcing," Journal of Fluid Mechanics, Vol. 371, 1998, pp. 21-58.
17. Kral, L. D., Donovan, J. F., Cain, A. B., and Cary, A. W., "Numerical Simulation of Synthetic Jet Actuators," AIAA Paper 97-1824, June-July 1997.
18. Joslin, R. D., Horta, L. G., and Chen, F.-J., "Transitioning Active Flow Control to Applications," AIAA Paper 99-3575, June-July 1999.
19. Joslin, R. D., and Viken, S. A., "Aerodynamic Performance of an Active Flow Control Configuration Using Unstructured-Grid RANS," AIAA Paper 2001-0248, January 2001.
20. Joslin, R. D., and Viken, S. A., "Baseline Validation of Unstructured Grid Reynolds-Averaged Navier-Stokes Toward Flow Control," Journal of Aircraft, Vol. 38, No. 2, pp. 389-393, Feb. 2001.
21. Arad, Erin, "Analysis of Boundary Layer Separation over a Bump Using Large Eddy Simulation," AIAA Paper 2001-2771.
22. Israel, David M., and Fasel, Hermann F., "Numerical Investigation of Compressible Effects on Active Control of Boundary Layer Separation,", AIAA Paper 2001-2771, June 2001.
23. Israel, D. M., and Fasel, H. F., "Numerical Investigation of Turbulent Separation Control Using Periodic Disturbances," AIAA Paper 2002-0409, January 2002.
24. Rallo, R., Dress, D. A., and Siegle, J. A., "Operating Envelope Charts for the Langley 0.3-Meter Transonic Cryogenic Wind Tunnel." NASA TM 89008, August 1986.
25. Wolf, S. W. D., "Evaluations of a Flexible Wall Testing Technique to Minimize Wall Interferences in the NASA Langley 0.3-Meter Transonic Cryogenic Tunnel," AIAA Paper 88-0140, January 1988.
26. Anderson, W. K., and Bonhaus, D. L., "An Implicit Upwind Algorithm for Computing Turbulent Flows on Unstructured Grids," Computers & Fluids, Vol. 23, No. 1, 1994, pp. 1-21.
27. Roe, P., "Approximate Riemann Solvers, Parameter Vectors, and Difference Schemes," J. of Comp. Phys., Vol. 43, 1981, pp. 357-372.
28. Spalart, P.R. and Allmaras, S.R.,: "A One-Equation Turbulence Model for Aerodynamic Flows," AIAA 92-0439, January, 1992.
29. Vatsa, V. N. Sanetrik, M. D. and Parlette, E. B. "A Multigrid Based Multiblock Flow Solver for Practical Aerodynamic Configurations," Frontiers of Computational Fluid Dynamics 1994, D. A. Caughey and M. M. Hafez, eds., John Wiley and Sons, 1994, pp. 413-447.
30. Bijl, H., Carpenter, M. H., Vatsa, V. N., "Time Integration Schemes for the Unsteady Navier-Stokes Equations," AIAA Paper 2001-2612, 2001.

31. Krist S. L., Biedron R. T., and Rumsey C. L., "CFL3D User's Manual (Version 5.0)", NASA TM-1998-208444, June 1998.
32. Marcum, D. L., "Generation of Unstructured Grids for Viscous Flow Applications," AIAA Paper 95-0212, January 1995.
33. Marcum, D. L., and Weatherhill, N. P., "Unstructured Grid Generation Using Iterative Point Insertion and Local Reconnection," AIAA Journal, Vol. 33, No. 9, September 1995.
34. White, Frank M., *Viscous Fluid Flow*, McGraw-Hill, New York, 1962.
35. Sreenivasan, K.R. "Laminarescent, relaminarizing, and retransitional flows", Acta Mechanica, Vol. 44, pp. 1-48, 1982.
36. Private Communications with L. Pack, 2002. Unpublished data of Seifert and Pack.
37. Patel, V. C., and Sotiropoulos, F., "Longitudinal Curvature Effects In Turbulent Boundary Layers," Prog. Aerospace Sci., Vol 33, pp. 1-70, 1997.
38. Spalart, Philippe R., "Trends in Turbulence Treatments," AIAA Paper 2000-2306, June 2000.

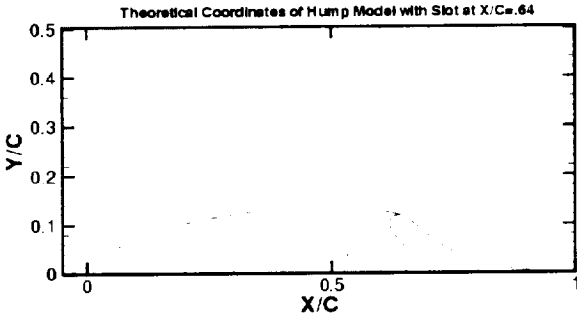

Figure 1. Theoretical coordinates of the hump model with slot location at X/C = 0.64

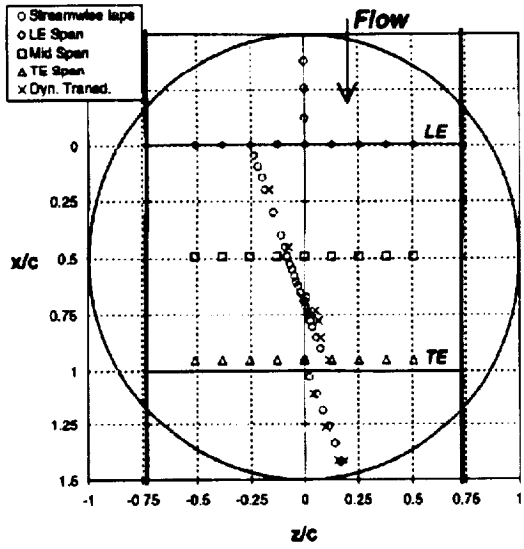

Figure 2. Top view of model, turntable, static and dynamic pressure tap locations, and end plates.

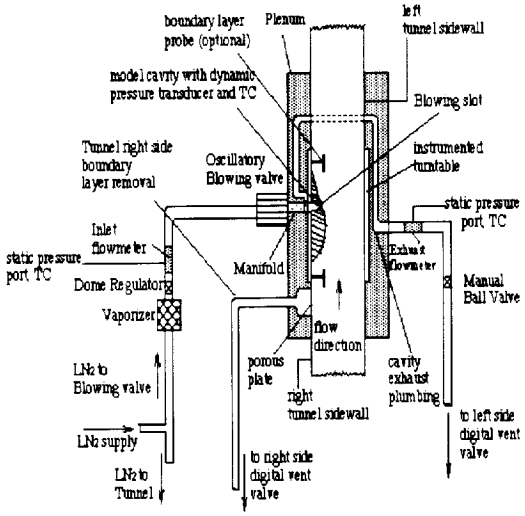

Figure 3. Schematic of experimental set-up in the 0.3m Transonic Cryogenic Tunnel.

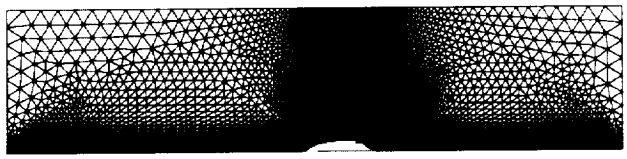

Figure 4. Unstructured grid generated within 0.3m Tunnel wall geometry with hump model (coarse grid).

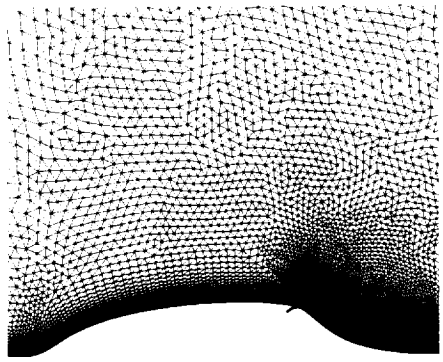

Figure 5. Enlarged view of the unstructured grid generated around the hump model (coarse grid).

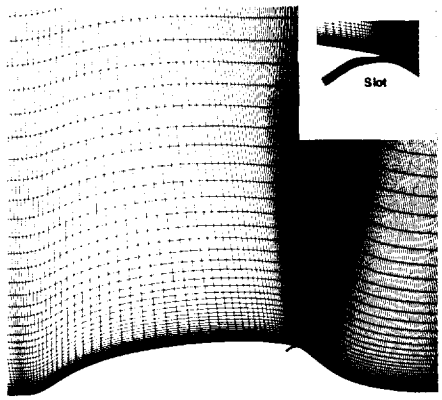

Figure 6. Enlarged view of the structured grid generated around the hump model (medium grid) with enlarged view of slot region.

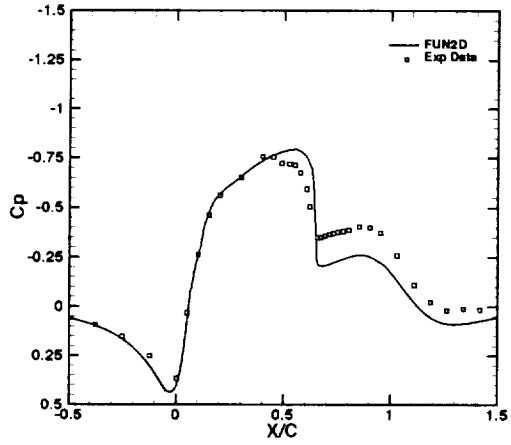

Figure 7. Baseline computational results versus experimental data using theoretical coordinates (M_∞ = 0.25; Re = 16 million).

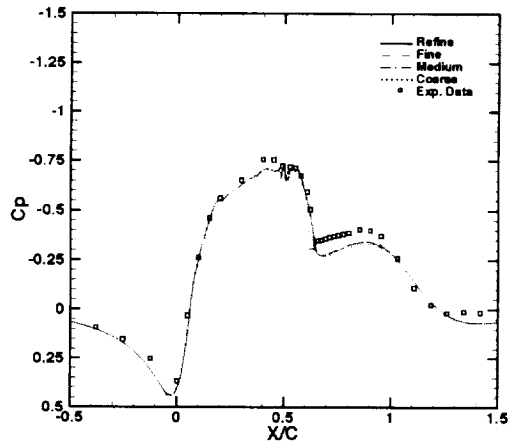

Figure 10. Baseline grid refinement study for FUN2D code (Cp distributions).

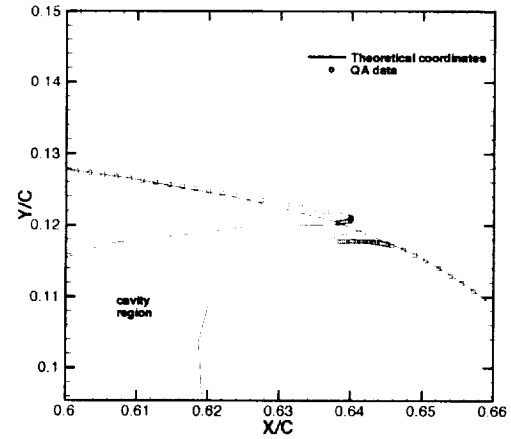

Figure 8. Comparison of theoretical coordinates with QA data near slot.

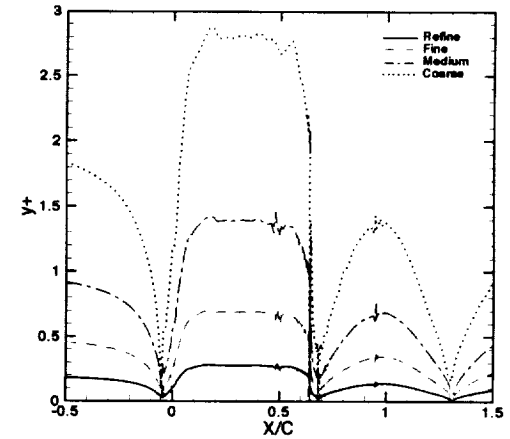

Figure 11. Baseline grid refinement study for FUN2D code (y^+ distributions).

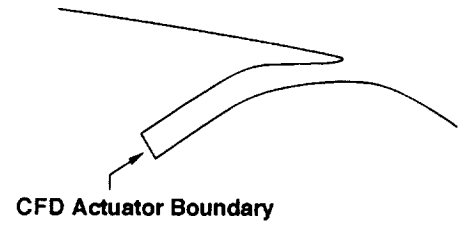

Figure 9. View of slot region used in the computations.

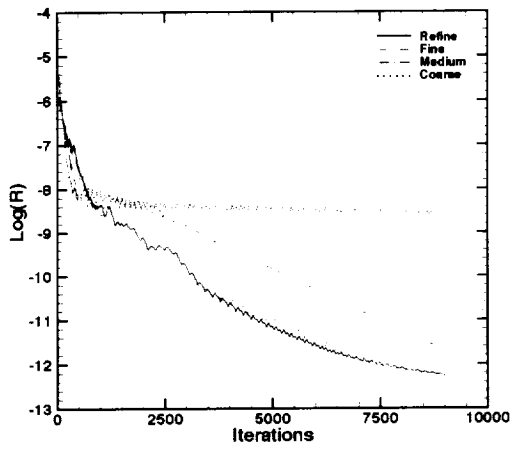

Figure 12. Baseline grid convergence study for FUN2D code (Log(residual)).

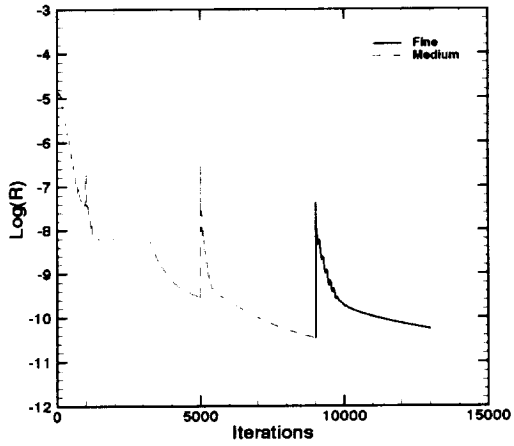

Figure 14. Baseline grid convergence study for CFL3D code (log(residual)).

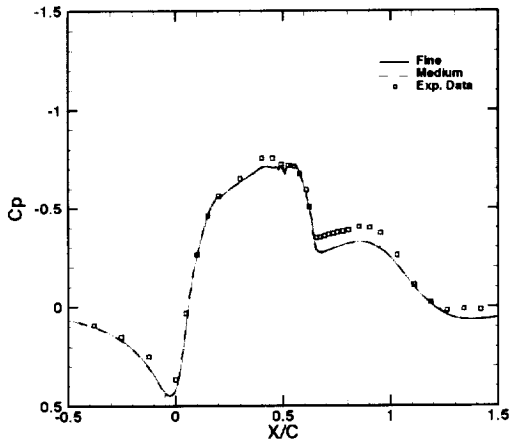

Figure 13. Baseline grid refinement study for CFL3D code (Cp distributions).

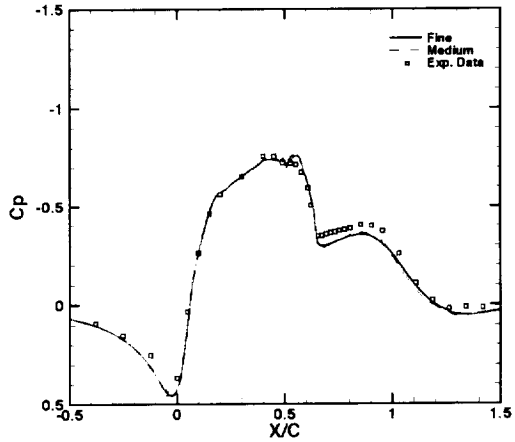

Figure 15. Baseline grid convergence study for TLNS3D (Cp distributions).

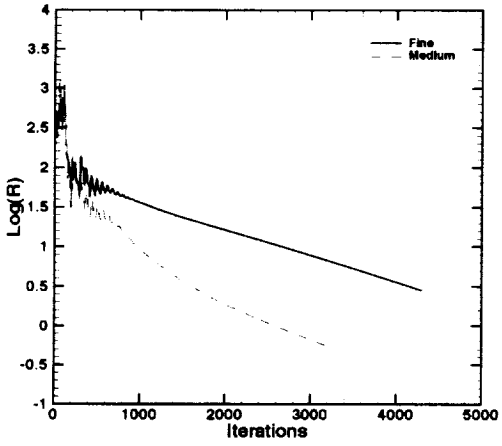

Figure 16. Baseline grid convergence study for TLNS3D code (log(residual)).

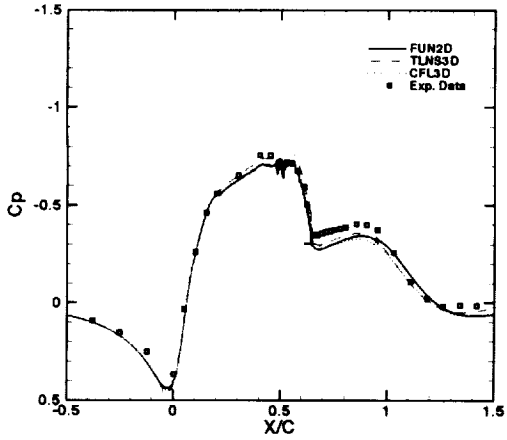

Figure 17. Baseline computational results versus experimental data(M_∞ = 0.25; Re = 16 million).

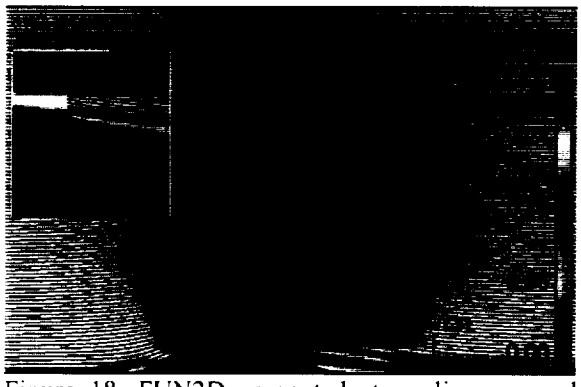

Figure 18. FUN2D computed streamlines around hump model (Baseline; M_∞ = 0.25; Re = 16 million).

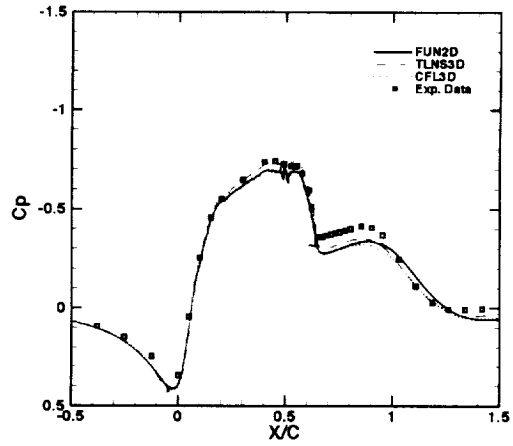

Figure 19. Baseline computational results versus experimental data (M_∞ = 0.25; Re = 4.2 million).

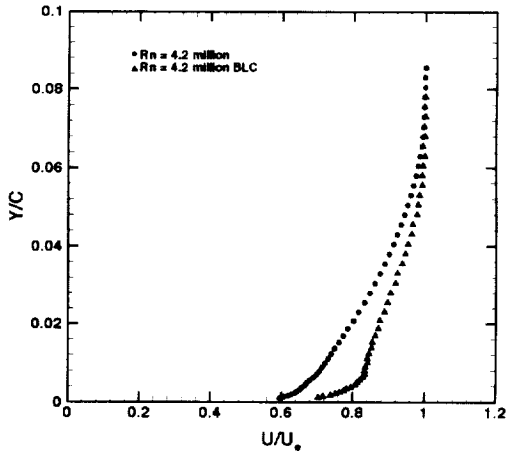

Figure 20. Experimental mean velocity profiles upstream of the model for the baseline and BLC (M_∞ = 0.25; Re = 4.2 million).

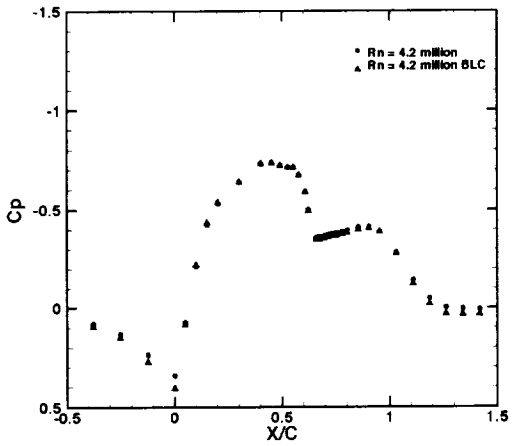

Figure 21. The effect of BLC upstream of the model on the uncontrolled model pressures (M_∞ = 0.25; Re = 4.2 million).

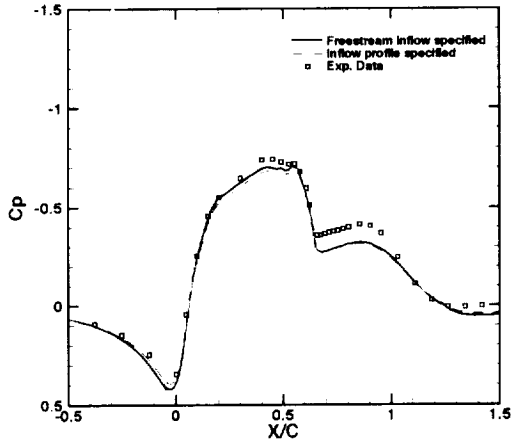

Figure 23. The effect of inflow velocity profile on the uncontrolled model pressures (M_∞ = 0.25; Re = 4.2 million).

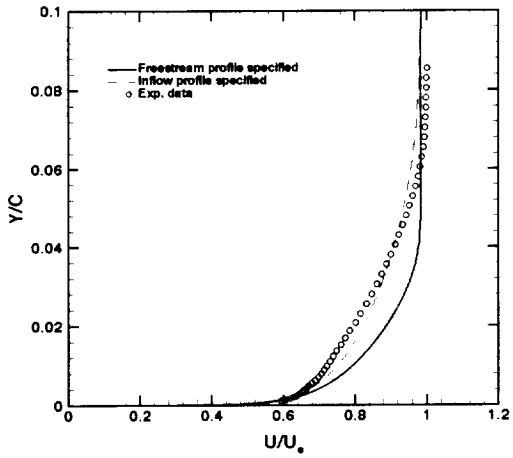

Figure 22. Velocity profiles calculated upstream of model when using freestream or specified inflow profile (M_∞ = 0.25; Re = 4.2 million).

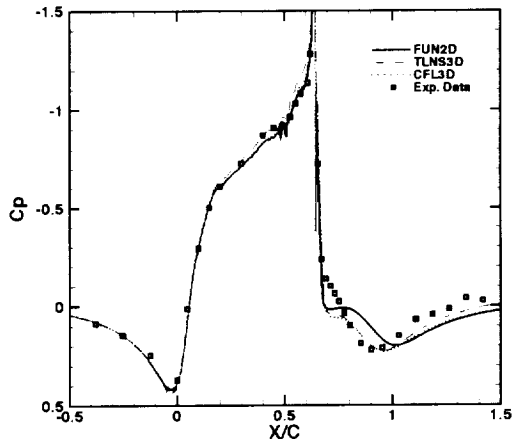

Figure 24. Computational results versus experimental data (M_∞ = 0.25; Re = 16 million; steady suction; c_μ = -0.76%).

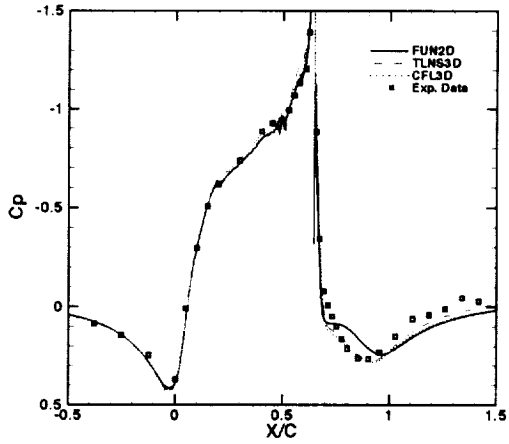

Figure 25. Computational results versus experimental data (M_∞ = 0.25; Re = 16 million; steady suction: c_μ = -1.4%).

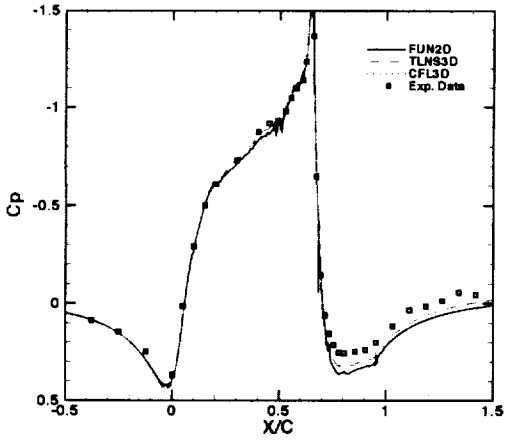

Figure 26. Computational results versus experimental data (M_∞ = 0.25; Re = 16 million; steady blowing; c_μ = 1.68%).

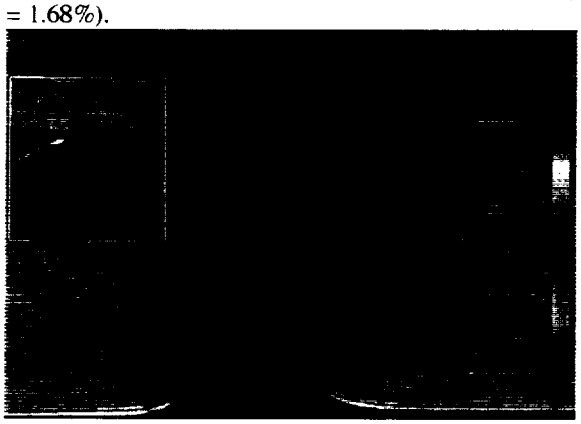

Figure 27. FUN2D computed streamlines around hump model (M_∞ = 0.25; Re = 16 million; steady blowing; c_μ = 1.68%).

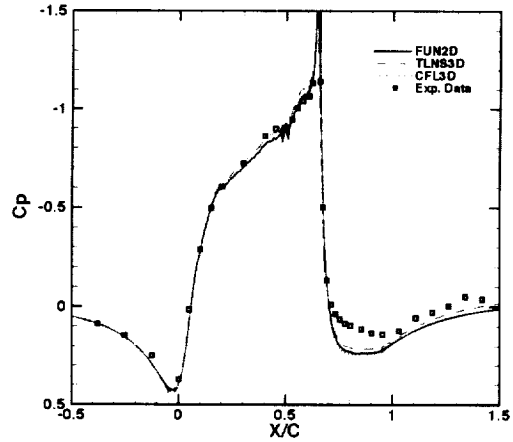

Figure 28. Computational results versus experimental data (M_∞ = 0.25; Re = 16 million; steady blowing; c_μ = 0.90%).

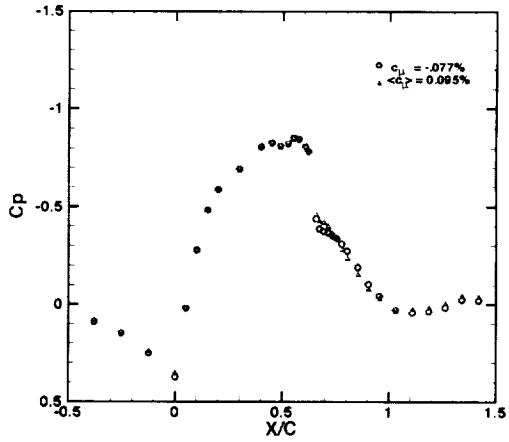

Figure 29. Mean pressures of the controlled flow using suction (c_μ = -0.077%) and periodic excitation ($<c_\mu>$ = 0.095%) at M_∞ = 0.25; Re = 16 million, F^+ = 1.6.

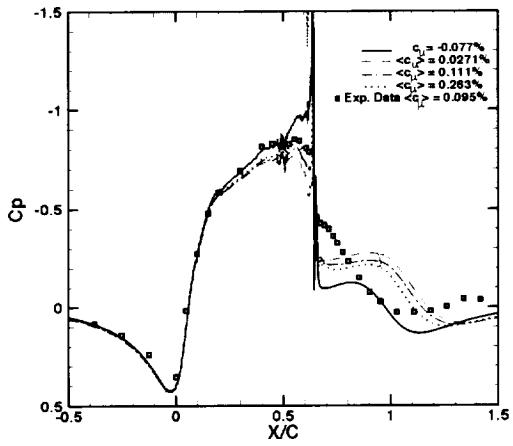

Figure 30. FUN2D mean pressures of the controlled flow using suction(c_μ = -0.077%) and range of $<c_\mu>$'s at M_∞ = 0.25; Re = 16 million, F^+ = 1.6.

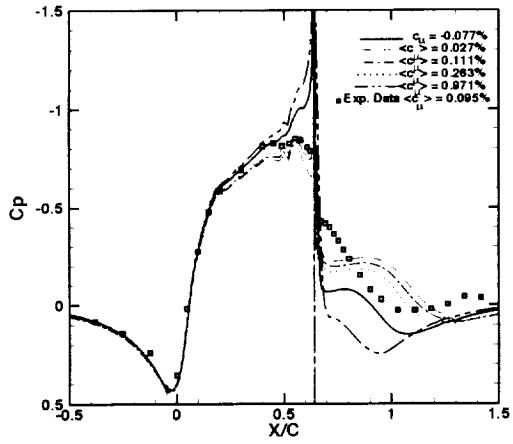

Figure 31. CFL3D mean pressures of the controlled flow using suction(c_μ = -0.077%) and range of $<c_\mu>$'s at M_∞ = 0.25; Re = 16 million, F^+ = 1.6.

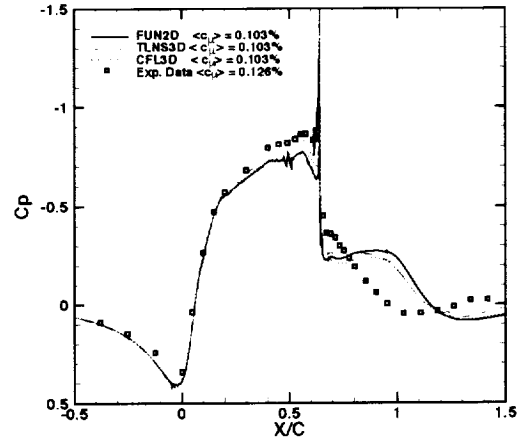

Figure 32. Computational results versus experimental data (M_∞ = 0.25; Re = 4.2 million; $<c_\mu>_{CFD}$ = 0.103%, F^+ = 1).

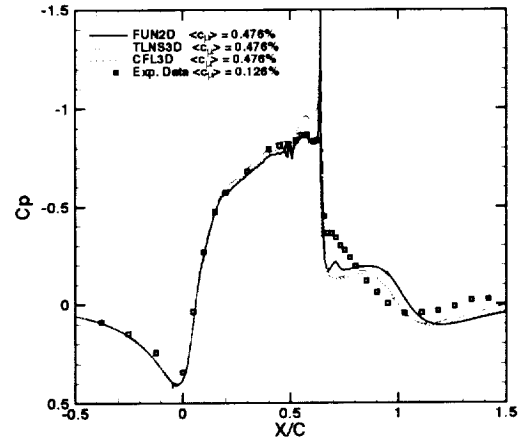

Figure 33. Computational results versus experimental data (M_∞ = 0.25; Re = 4.2 million; $<c_\mu>_{CFD}$ = 0.476%, F^+ = 1).

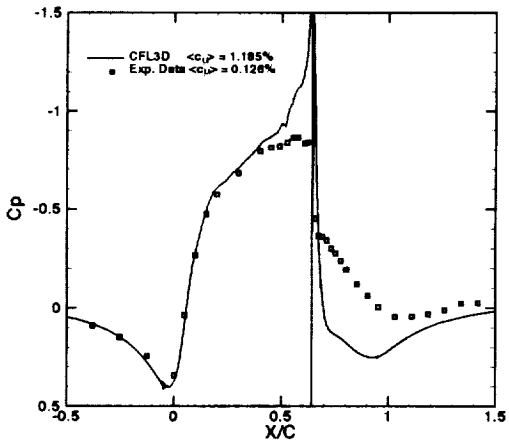

Figure 34. Computational results versus experimental data ($M_\infty = 0.25$; Re = 4.2 million; $\langle c_\mu \rangle_{CFD} = 1.185\%$, $F^+ = 1$).

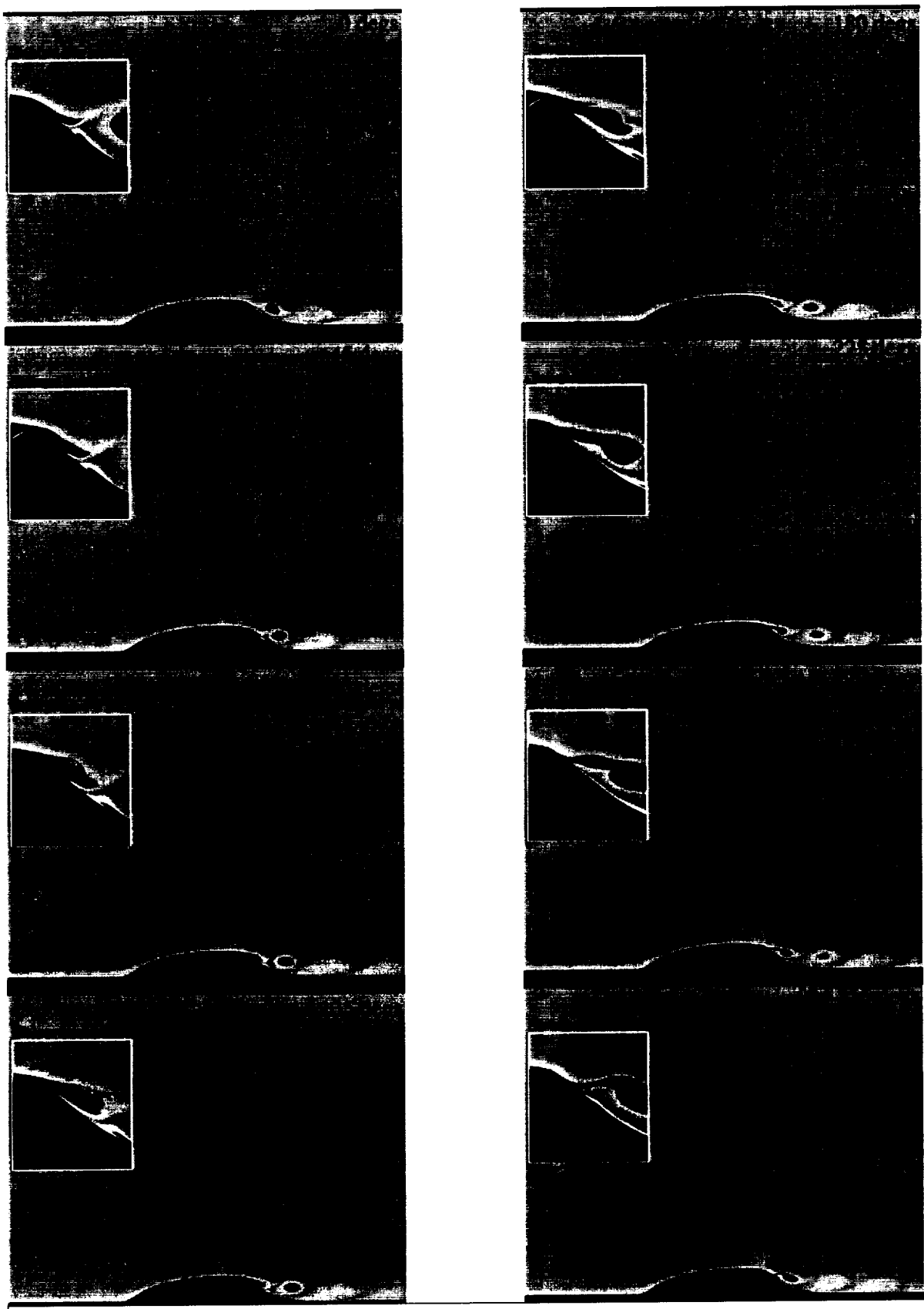

Figure 35. Vorticity plots for one actuator cycle with FUN2D($M_\infty = 0.25$; Re = 4.2 million; $\langle c_\mu \rangle = 0.476\%$)

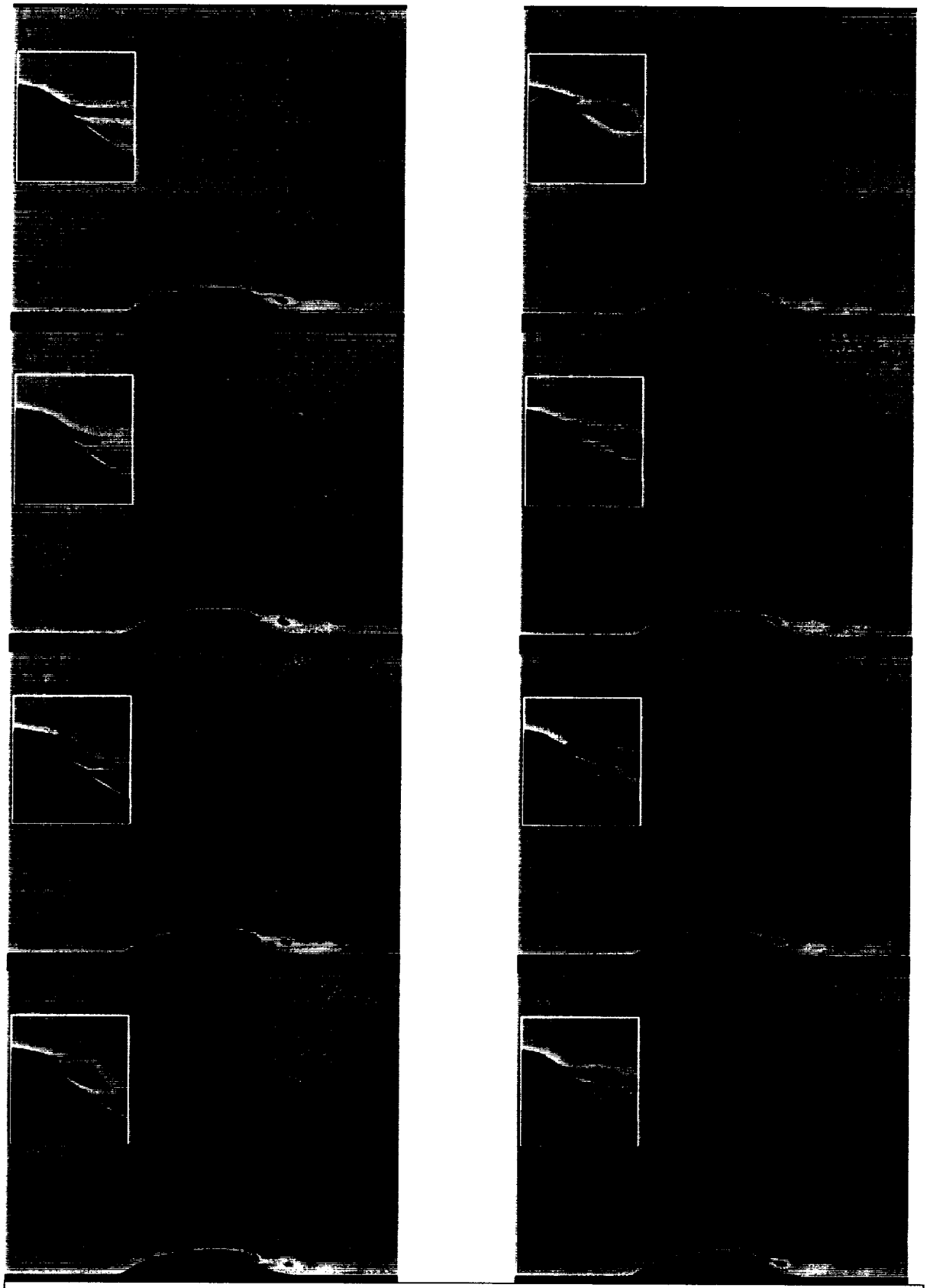

Figure 36. Vorticity plots for one actuator cycle with CFL3D(M_∞ = 0.25; Re = 4.2 million; $\langle c_\mu \rangle$ = 0.476%)

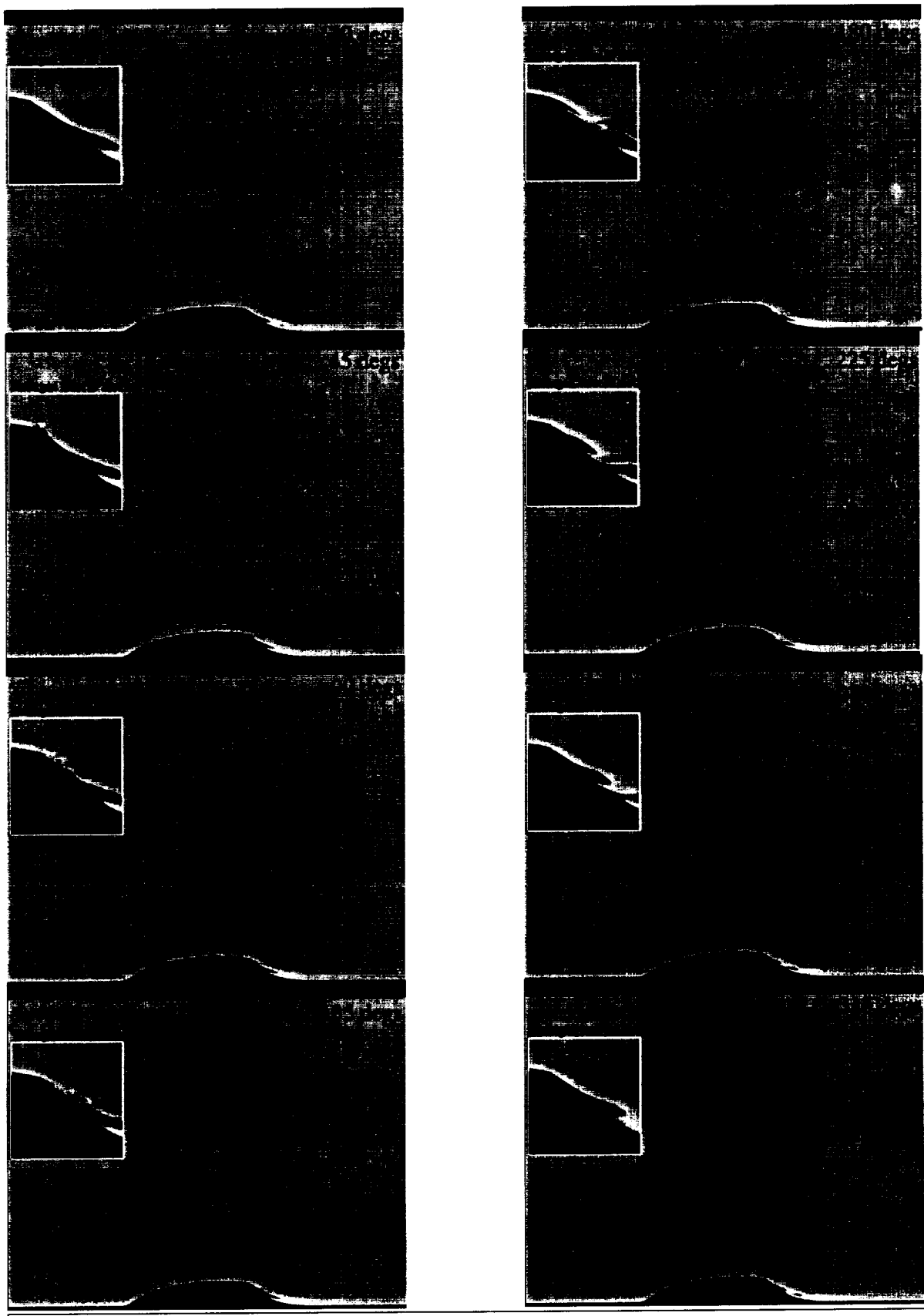

Figure 37. Vorticity plots for one actuator cycle with CFL3D(M_∞ = 0.25; Re = 4.2 million; $\langle c_\mu \rangle$ = 1.185%)